ELECTROMOTION

Volume 17, Number 3
July – September 2010

Contents

Special Issue: Papers presented at the *5th International Conference and Exhibition on Ecological Vehicles and Renewable Energies – EVER' 10*
25-28 March 2010, Monte-Carlo, Monaco
and selected for publication in 'ELECTROMOTION' quarterly by the *EVER' 10 Program Committee*

Guest Editorial		135
J. Junak, G. Ombach	Brushless motors for automotive applications with different on-board voltage levels	137
T. Finken, M. Hafner, M. Felden, K. Hameyer	Design rules for energy-efficient interior permanent-magnet synchronous motors in hybrid electric vehicle applications	143
D. Ilea, M.M. Radulescu, F. Gillon, P. Brochet	Particle-swarm-optimized design of a three-phase full-bridge inverter-fed switched reluctance motor	155
R. Trabelsi, A. Khedher, M.F. Mimouni, F. M'Sahli, A. Masmoudi	Rotor flux estimation based on nonlinear feedback integrator for backstepping-controlled induction motor drives	163

D. Casadei, M. Mengoni, G. Serra, C. Rossi, A. Tani, L. Zari	Comparison of control schemes for induction motor drives in electric vehicle applications	173
G. Waltrich, J.L. Duarte, M.A.M. Hendrix, J.J.H. Paulides	Three-port bi-directional converter for electric vehicles: focus on high-frequency coaxial transformer	183
O. Hegazy, J. Van Mierlo	A novel eight-switch inverter topology for plug-in hybrid electric vehicle	191
B. El Badsi	Space-vector pulse-width modulation strategies devoted to the control of reduced-structure inverter-fed induction motor drives	209
F. Kurokawa, Y. Maeda, Y. Shibata, H. Maruta, T. Takahashi, K. Bansho, T. Tanaka, K. Hirose	A new fast-response digital control process for switching power supply	220
C. Zhou, K. Qian, M. Allan, W. Zhou	An analysis of the cost of vehicle-to-grid with consideration of electric-vehicle battery cycle life	226

ELECTROMOTION Agenda 2010 - 2011 142

Design rules for energy-efficient interior permanent-magnet synchronous motors in hybrid electric vehicle applications

T. Finken, M. Hafner, M. Felden and K. Hameyer

Abstract *– Permanent-magnet excited synchronous machines (PMSM) are particularly well-suited to high power density and high overall efficiency applications. These are precisely two important requirements for drives implemented in parallel hybrid electric vehicles. In this case, there is, however, an additional important requirement, namely, that due to a lack of space in the drivetrain, the outer dimensions of the electrical machine is strictly limited. Because of this additional condition, conventional design rules need to be reconsidered and reorganized appropriately. The paper presents a methodology to optimize the operational efficiency of PMSM drives under limited installation space.*

Keywords: interior permanent-magnet synchronous motor, energy efficiency, hybrid electric vehicle, drivetrain

1. Introduction

An increasing awareness on ecological issues and the fossil-fuel shortage are strong incentives to develop more efficient vehicles, with lower fuel consumption but without reducing driving comfort. The hybrid electric vehicle (HEV), which combines the drive power of an internal combustion engine and that of one or several electrical machines, is a promising concept in this regard.

Due to the limited available space and the high demands in power density and overall efficiency, the permanent magnet synchronous machine (PMSM) is the mainly applied machine type in parallel hybrid electric vehicles [1]-[6]. The desired reduction of the vehicle's fuel consumption requires a good overall efficiency and thus losses as low as possible.

Since such machines are not operated at one particular operation point but at a complete range of operation points, they must be designed with regard to the intended application. Thus, in a first step the operating range of these machines are estimated in view of the future application.

Firstly, the frequency distributions of the operation points resulting from vehicle simulations and defined driving cycles must be determined. In a next step, the electrical machine must be designed in such a way, that the range of best efficiency meets the range of most frequent operation points, i.e. the average overall efficiency must be maximized in order to improve the energy balance and reduce the vehicle's fuel consumption.

Furthermore, the installation space available for the electrical machine is often very limited, especially in the case of parallel hybrid electric vehicles in which the electrical machine is integrated into the drivetrain, often between combustion engine and transmission. Due to this integration, the issue of the machine design is rather the question "How much power can be integrated into that specific space?" than "How can we get that specific power into the available space?".

In this case, electrical machine design is often conducted under the constraint that the outer dimensions of the machine are fixed - the degrees of freedom are the pole-pair number, the rotor radius and the type of winding.

This paper presents an approach to determine the optimal rotor radius, the optimal pole pair number and the appropriate winding type of the machine, regarding the machine's rated power, overload capacity and average efficiency, which

ELECTROMOTION

Volume 17, Number 3
July – September 2010

Contents

Special Issue: Papers presented at the *5th International Conference and Exhibition on Ecological Vehicles and Renewable Energies – EVER' 10*
25-28 March 2010, Monte-Carlo, Monaco
and selected for publication in 'ELECTROMOTION' quarterly by the *EVER' 10 Program Committee*

Guest Editorial		135
J. Junak, G. Ombach	Brushless motors for automotive applications with different on-board voltage levels	137
T. Finken, M. Hafner, M. Felden, K. Hameyer	Design rules for energy-efficient interior permanent-magnet synchronous motors in hybrid electric vehicle applications	143
D. Ilea, M.M. Radulescu, F. Gillon, P. Brochet	Particle-swarm-optimized design of a three-phase full-bridge inverter-fed switched reluctance motor	155
R. Trabelsi, A. Khedher, M.F. Mimouni, F. M'Sahli, A. Masmoudi	Rotor flux estimation based on nonlinear feedback integrator for backstepping-controlled induction motor drives	163

D. Casadei, M. Mengoni, G. Serra, C. Rossi, A. Tani, L. Zari	Comparison of control schemes for induction motor drives in electric vehicle applications	173
G. Waltrich, J.L. Duarte, M.A.M. Hendrix, J.J.H. Paulides	Three-port bi-directional converter for electric vehicles: focus on high-frequency coaxial transformer	183
O. Hegazy, J. Van Mierlo	A novel eight-switch inverter topology for plug-in hybrid electric vehicle	191
B. El Badsi	Space-vector pulse-width modulation strategies devoted to the control of reduced-structure inverter-fed induction motor drives	209
F. Kurokawa, Y. Maeda, Y. Shibata, H. Maruta, T. Takahashi, K. Bansho, T. Tanaka, K. Hirose	A new fast-response digital control process for switching power supply	220
C. Zhou, K. Qian, M. Allan, W. Zhou	An analysis of the cost of vehicle-to-grid with consideration of electric-vehicle battery cycle life	226

ELECTROMOTION Agenda 2010 - 2011 142

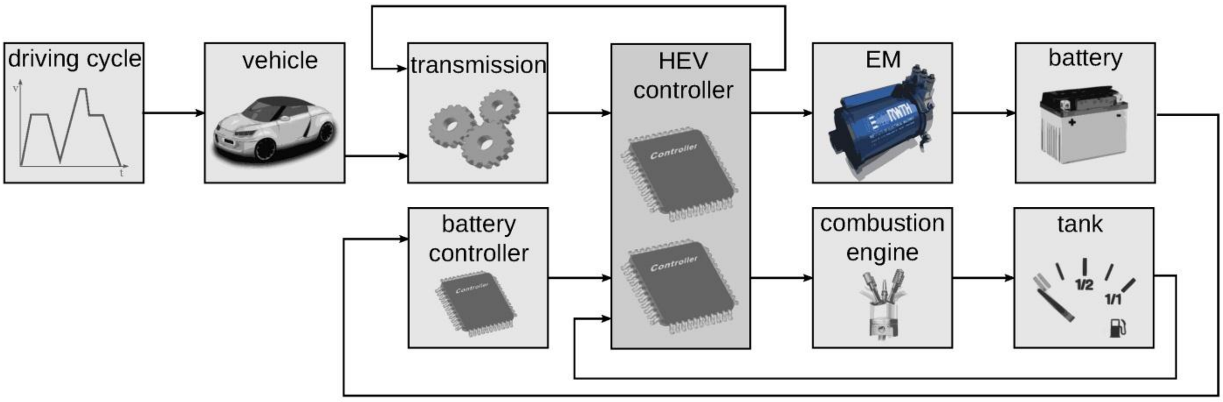

Fig. 1. Vehicle model for a parallel HEV.

depends on above-named vehicle simulations. The analysis includes the calculation of all losses: iron losses, Ohmic losses and eddy-current losses in the permanent magnets.

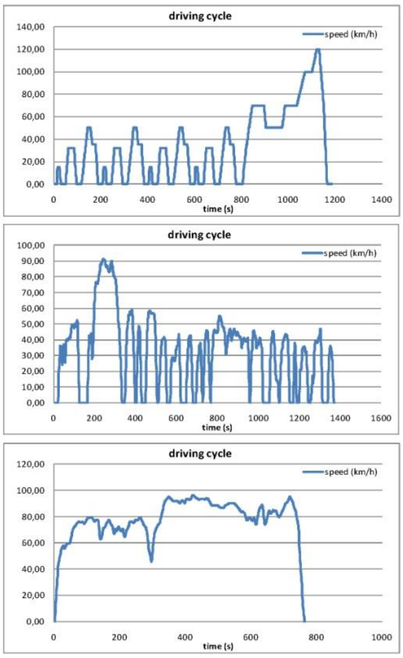

NEDC

time : 1184 s
distance : 10.93 km
max. speed : 120 km/h
avg. speed : 33.21 km/h
max. accel : 1.06 m/s^2
max. decel : -1.39 m/s^2

UDDS

time : 1369 s
distance : 11.99 km
max. speed : 91.25 km/h
avg. speed : 31.51 km/h
max. accel : 1.48 m/s^2
max. decel : -1.48 m/s^2

HWFET

time : 765 s
distance : 16.51 km
max. speed : 96.4 km/h
avg. speed : 77.58 km/h
max. accel : 1.43 m/s^2
max. decel : -1.48 m/s^2

Fig. 2. Exemplary driving cycles.

2. Vehicle simulation

The main requirements on electrical machines applied in (hybrid) electric vehicles are: a high overall efficiency within a large range of the torque-speed characteristic, a high overload capacity, small installation space and weight and a high reliability at low cost.

But to improve the energy balance and reduce fuel consumption, the electrical machine must be specifically designed in view of the characteristic of the considered powertrain, i.e. the overall efficiency must be optimized over the range of actually used operation points. Vehicle-simulation models (Fig.1) are used, to determine the expected operation points. They combine driving cycles, the vehicle data, the transmission, the battery, the battery controller and the main vehicle control unit.

A driving cycle is a series of data points representing the speed of a vehicle versus time. For machine design purposes, an average driving cycle should be generated, which includes weighted parts of urban, extra urban and highway driving cycles according to the vehicle's intended purpose. The vehicle model itself should account for its mass, drag coefficient and friction losses. Transmission ratios and their efficiencies are described by the transmission submodel. The hybrid electric vehicle controller, monitoring all conditions, controls all components regarding driving and control strategies.

The results from these vehicle simulations can be among others the fuel consumption, the energy balance, the battery's state of charge and the frequency distribution of the electrical machine's operation points (Fig.3). It is to be considered: the more detailed the vehicle model, the better the prediction of expected operation points, which are required for the choice of machine type and the machine design.

In this study, three driving cycles and two hybrid concepts are used to demonstrate how the frequency distributions is affected. Exemplary driving cycles are the New European Driving Cycle (NEDC), the Urban Dynamometer Driving

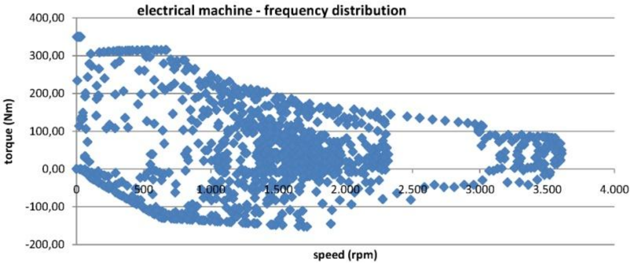

(a) UDDS, series HEV

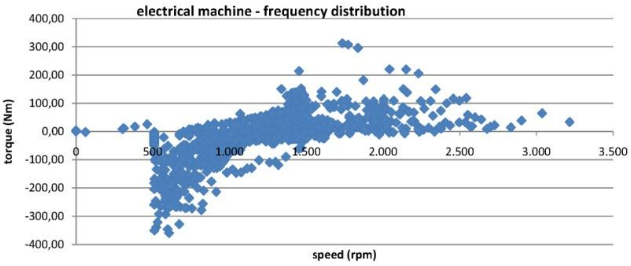

(b) UDDS, parallel HEV

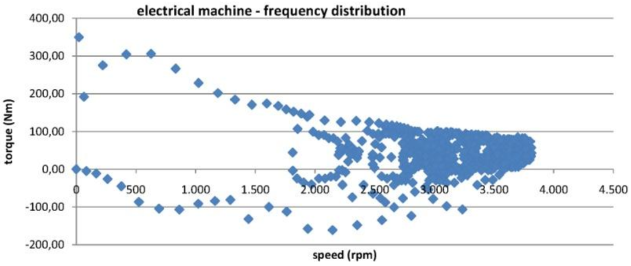

(c) HWFET, series HEV

Fig. 3. Exemplary frequency distributions.

Schedule (UDDS), and the EPA Highway Fuel Economy Cycle (HWFET), Fig.2.

The hybrid vehicle concepts under analysis are the parallel hybrid vehicle and the series hybrid vehicle. The electrical machine's operation points in a parallel HEV depend on the strategy of the hybrid control unit and on the vehicle's transmission. Since the electrical machine is only used in addition to the internal combustion engine, it has not to be designed for the full vehicle power. The rotational speed and the requested torque may be restricted to a limited range in this case. On the contrary, the machine applied in a series HEV has to provide the total drive power and therefore has to be designed for a wide torque- and speed range.

Typical frequency distributions for the considered vehicle concepts and driving cycles are depicted in Fig.3. Compared to the series HEV, the operation points of the parallel HEV are limited to a smaller speed range, due to its automatic transmission.

On the other hand the differences between the driving cycles become apparent. The UDSS requires the highest torques, especially at lower speeds, due to frequent accelerations and brakings in urban environment. The HWFET results in a frequency operation mostly limited to a range of high speed and low torque range, resulting from the constant high speed of the highway driving cycle.

3. Numerical calculation methods

Since the design process of PMSMs has to consider saturation- and flux-leakage effects, which cannot be determined accurately by analytical formulae, quasi-static numerical FE simulations are performed for each geometry. All simulations were conducted with the in-house FEM software *iMOOSE* [7].

First, a ***No-Load Simulation*** is performed to calculate the stator flux-linkage and the back-emf. In addition, the magnetic flux distribution is visualized.

To determine the overload capability of studied geometries, a ***Demagnetization Test*** is conducted. The worst case would be a fault in the power electronics and control, feeding the maximum current into negative direct axis ($I_d = -I_{max}$). The demagnetization of the permanent magnets, which is maximum then, must not cause irreversible demagnetization. In order to determine this limit, a current is fed in negative direct axis and the current density stepwise increased to determine the maximum current I_{max}, still having the working point on the linear part of the demagnetization characteristic.

The torque of an IPMSM ($X_q > X_d$) can be determined by:

$$T = \frac{3p}{\omega}\left[U_p - I_d \cdot \left(X_q - X_d\right)\right] \cdot I_q . \qquad (1)$$

It consists of the synchronous torque T_{syn} and, due to the saliency of the IPMSM, the reluctance torque T_{rel}:

$$T = \frac{3p}{\omega} \cdot U_p I_q - \frac{3p}{\omega} \cdot I_q I_d \cdot \left(X_q - X_d\right) = T_{syn} - T_{rel} \qquad (2)$$

With $I_q = I \cos\psi$, $I_d = I \sin\psi$ and the field-weakening angle ψ, the torque can be written as:

$$T = \hat{T}_{syn}\cos(\psi) - \hat{T}_{rel}\sin(2\psi) \qquad (3)$$

This means the torque depending on the field-weakening angle consists of a fundamental ($\hat{T}_{syn}$) and the first harmonic ($\hat{T}_{rel}$). The field-weakening, angle at the which the sum of the synchronous torque and the reluctance torque (and thus the available total torque) is maximum, is called the optimum field-weakening angle $\psi = \psi_{opt}$ (Fig.4).

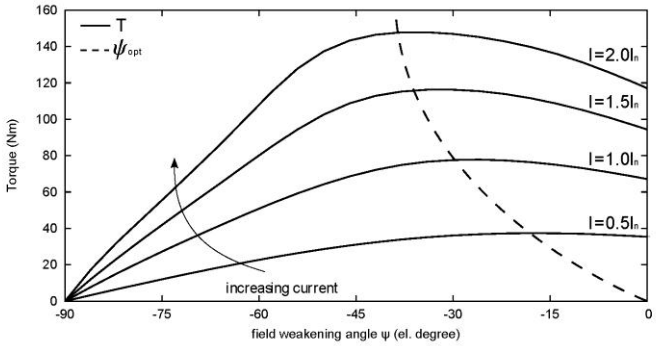

Fig. 4. The average torque over ψ, resulting from the ”locked-rotor test".

The so called ***"Locked-Rotor Test"*** is used to determine the absolute value of the synchronous torque $\hat{T}_{syn}$, the absolute value of the reluctance torque $\hat{T}_{rel}$, the optimum field-weakening angle ψ_{opt} and the resulting maximum torque. This calculation is performed for a stepwise increasing stator-current density in order to determine how those quantities depend on the load current.

The direct- and quadrature-axis inductances (L_d and L_q) are calculated by means of the ***LdLq-Computation*** as a function of the load current and the field weakening angle ψ. The inductances L_d and L_q are required to determine the field weakening capability and to determine the torque for each operation point by the torque equation (1). For this reason the inductances are required for the machine's control, especially in the range of field weakening.

In order to minimize fuel consumption, the efficiency of the drive must be carefully optimized and, therefore, all losses need be accurately evaluated for all operation points. This computation is conducted by the ***Operation Point Simulation***. At this step, the optimum field-weakening angle ψ_{opt} is used to set the maximum torque in the range of base speed, whereas ψ has to be set by means of control strategies in the range of field weakening.

Ohmic losses are estimated taking end windings into account. Iron losses are computed by means of quasi-static numerical FE simulations and an improved post-processing formula based on the loss-separation principle [8]-[10], and that considers rotational hysteresis losses as well. The eddy-current density in the permanent magnets is calculated by means of a transient 3D-FE approach, as described in [11]-[12]. The eddy-current density and the specific conductivity of the magnet material are used to determine the eddy-current losses by integration over the magnet's volume.

With performed loss calculation it is possible to determine the total losses for all operation points (i.e. as a function of speed and torque). Resulting from the total losses and the output power, the efficiency can be calculated. The results are depicted in two-dimensional maps: the loss maps and efficiency maps.

Furthermore, the ***Operation Point Simulation*** calculates the *T(t)*-characteristics and with that, by means of a FFT, the torque's harmonic content - the torque ripple.

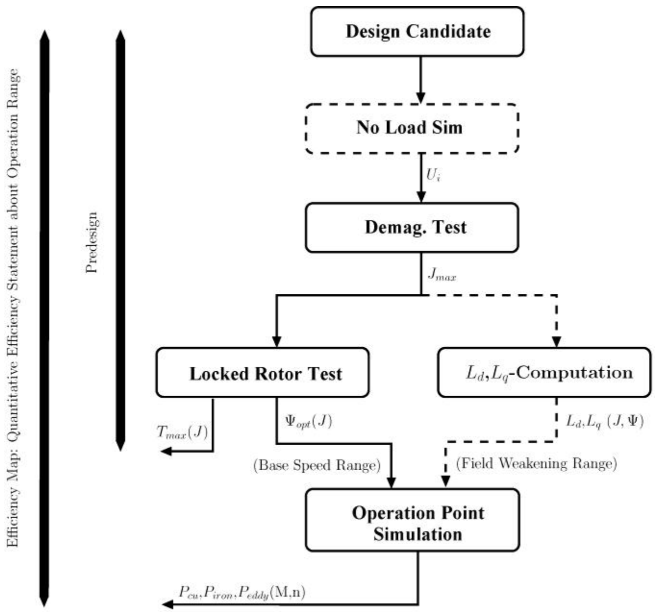

Fig. 5. Flowchart of the automated design process for the PMSM.

The huge amount of FE computations required for described analysis leads to a high computational time and an additional time-consuming evaluation effort for the design engineer. Therefore, all proposed design procedures have been combined into an automated tool chain (Fig.5), so that the machine characteristics of several design candidates can be computed independently in parallel. Afterwards they are compared with each other to determine the optimal parameter set combination.

4. Initial design approach

Electrical machines are usually dimensioned by means of analytical formulae. In particular, the stator diameter is directly derived from the value of the nominal power [13],[14]. But if the available installation space is limited and the outer dimensions are fixed, the approach must be different. There are two main degrees of freedom: rotor diameter *D* and the number of pole pairs *p*.

a) The variation of the rotor diameter

The first degree of freedom is the rotor diameter D, whereas the stator diameter D_S remains constant.

A given force produces a torque proportional to the radius, i.e. the torque is at least linearly proportional to the diameter. Moreover, if the diameter increases, there is more space for magnets around the rotor which increases the specific magnetic loading. Therefore, torque and power increase with the diameter. But increasing the rotor diameter lowers the volume of the stator. The area available for current injection decreases then, and if a constant current density is assumed, the specific electric loading A decreases as well. As a result, a maximum of the torque can be expected for an intermediate value of the rotor diameter D.

From analytical considerations (Fig. 6), the average tangential force F_α can be calculated from the air-gap field by means of the Maxwell Stress Tensor:

$$F_\alpha = \oint_F B_n H_t dF = \frac{lD^2}{2}\int_0^{2\pi} B_n H_t d\alpha \qquad (4)$$

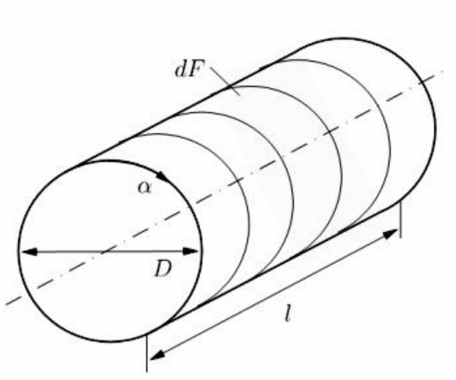

Fig. 6. Geometrical parameters of the rotor.

With the simplification $B_n = B(\alpha)$ and $H(t) = \frac{I}{l} = A(\alpha)$, the torque T is given by:

$$T = \frac{D}{2}F(\alpha) = \frac{lD^2}{4}\int_0^{2\pi} B(\alpha)H(\alpha)d\alpha \qquad (5)$$

The specific electric loading *A* is proportional to the stator area available for current injection and to the current density *J*:

$$A \sim \frac{I_{tot}}{\pi D} \sim \frac{J}{\pi D}\left[\pi\left(\frac{D_S}{2}\right)^2 - \pi\left(\frac{D}{2}\right)^2\right] \qquad (6)$$

Therefore, the torque is proportional to:

$$T \sim D^3\left(\frac{D_S^2}{D^2} - 1\right) = DD_S^2 - D^3. \qquad (7)$$

If the fixed outer diameter is $D_S = 270$mm, the normalized torque reaches its maximum at about D = 156mm (radius r = 78mm), as depicted in Fig.7. Therefore a detailed study, of how this variation affects the machine's parameters, is conducted in the range of r = 60mm to r = 95mm.

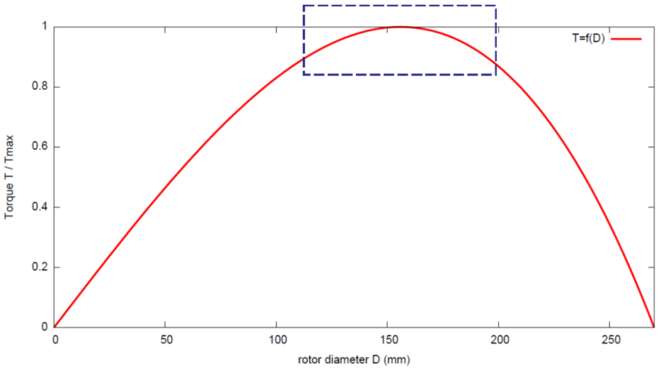

Fig. 7. The normalized torque depending on the rotor diameter D.

b) The variation of the pole-pair number

Another degree of freedom is the pole pair number *p*. The pole-pair number influences the rotor size and thus the volume of a machine when using analytical formulas - increasing the poles increases the force generated by the motor. Furthermore, the stator-yoke height and the length of the end winding take up less space with increasing pole pair number, so the active length of the motor can be enlarged to reach the fixed total length (Fig.8). Thus, the power density increases with increasing power at constant volume.

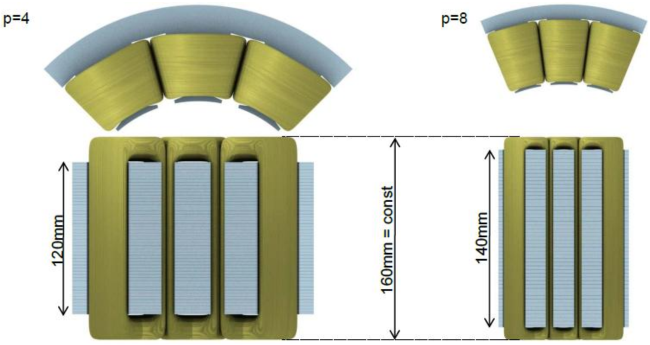

(a) Concentrated winding

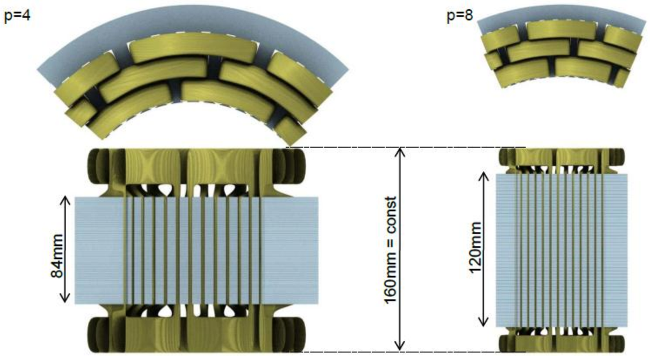

(b) Distributed winding (q=2)

Fig. 8. The active length depending on p.

However, increasing the number of poles implies decreasing the magnet width and increasing the amount of magnet leakage flux, which in turn reduces the air gap flux density. So, the force will not increase indefinitely but will, from a certain point on, decrease with a further increase of magnet poles. Thus, there is an optimum number of magnet poles.

Moreover, iron losses increase more than linearly with frequency, and the higher the pole pair number the higher the frequency of the stator currents and of the alternating magnetic field. Iron losses are the dominant losses in PMSMs at high rotational speeds. So the total losses increase significantly with increasing pole number at this speed range and thus the overall efficiency decreases.

5. Numerical-aided design approach

Since the effect of the pole pair number can not be determined accurately by analytical formulae (due to the influence of flux leakage and iron losses as discussed above), numerical FE simulations are performed. A matrix of geometrical variants (Fig. 9) [p=4..8, D=120..210mm] is established in order to study the effect of pole pair variation, as well as to verify the analytical estimation of the optimal rotor diameter.

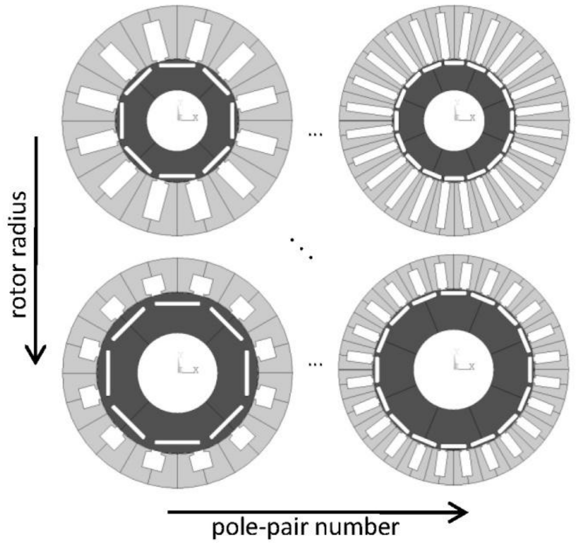

Fig. 9. The matrix of *D*- and *p*-variations.

5.1. Simulation models and different stator types

This analysis is performed on several stator types, one with a concentrated winding (CW) and two with distributed windings (DW) and different distribution factor *q* (slot/pole ratio, *q*=1 and *q*=2; Fig. 10). Both winding types have their own advantages and disadvantages [15]-[17].

Compared to distributed windings, concentrated windings reduce the dimensions of the coil ends and extends the possible active length of the machine, so the power density is higher than that of machines with distributed

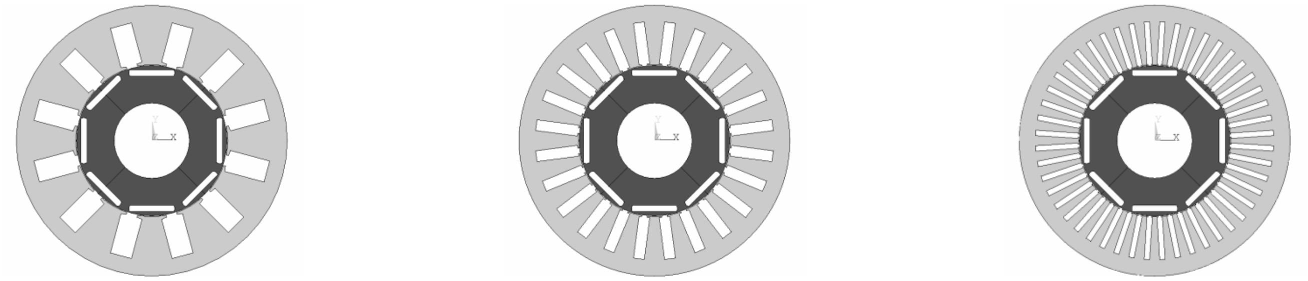

(a) CW **(b)** DW (q=1) **(c)** DW (q=2)

Fig. 10. Stator types.

windings. In addition, Ohmic losses related to the output power are reduced, because end windings do not contribute to the torque generation but generate thermal heat by copper losses. Moreover, concentrated windings significantly increase the copper fill factor (up to f_{cu}=70%) and extends the automated manufacturing because rectangular conductors, preformed coils and segmented cores are possible to apply.

Distributed windings feature better winding factors than concentrated windings, so machines with distributed windings require a smaller number of turns, but its end windings take up more space and the winding volume increases. Furthermore, the copper fill factor is less compared to concentrated windings (up to f_{cu}=50%), as this winding type has to be produced as moved-in winding. The main advantage of the distributed winding is the possibility to vary the slot/pole ratio (zoning) and to apply short-pitching. By zoning (spreading a coil onto multiple slots q) and short-pitching (displacement of single or several turns into slots nearby) harmonics of the magnetic field can be weakened. So the iron losses depending on these harmonics are lower than that of machines with concentrated windings.

The simulation of the geometry variations was performed with following parameters, which remain constant for all geometries: the axial total length l = 160mm, the outer stator diameter D_S=270mm and an air gap of δ = 0.7mm. The nominal current density the copper was set to the maximum allowed value in an air-cooled machine, i.e. J_n = 6A/mm^2, the copper fill factor to f_{cu}=0.6 using the concentrated winding and f_{cu} = 0.5 using the distributed winding.

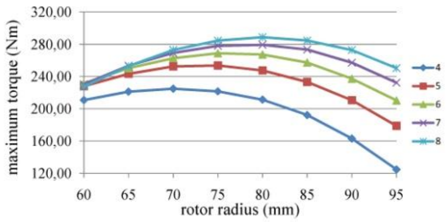

(a) CW, $I = I_n$

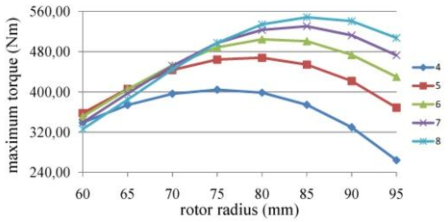

(b) CW, $I = 2I_n$

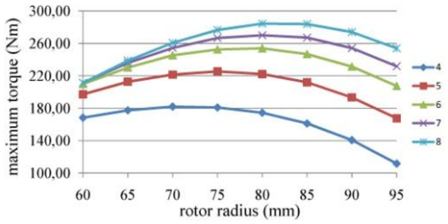

(c) DW (q=2), $I = I_n$

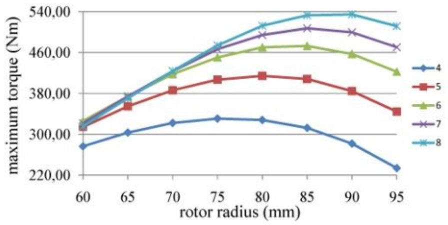

(d) DW (q=2), $I = 2I_n$

Fig. 11. Maximum torque depending on p and rotor radius.

5.2. Determination of the optimum rotor radius

As described in the previous section, the optimum rotor radius is determined for each pole-pair number *p* and winding. The maximum torque depending on rotor radius and pole-pair number is depicted in Fig.11 (exemplary for CW and DWq2) taking into account the possible scaling of the active length as described.

The torque characteristics and their maxima approximately meet the analytical estimation. However, one can recognize as a general rule that the torque's maximum shifts towards higher rotor radii by increasing the load current or increasing the pole-pair number. Moreover, the maximum of the torque curve reaches a maximum when increasing the pole-pair number, so that the torque (and thus the output power) can not be raised indefinitely by increasing the pole-pair number.

5.3. Choice of the pole number and winding type

In the previous section, the optimum rotor radius was determined for each pole-pair number. Before choosing the pole-pair number and the winding type, the effects of these variations have to be studied in detail. In the following the results of this study are presented by means of two geometries demonstrating the effect in a good way.

The results are depicted in loss- or efficiency maps, in which the full line marks the line of rated torque and the dashed line represents the maximum torque.

a) Ohmic losses

In Fig.12 the Ohmic-loss maps are depicted for the geometries CW-p6rra80 (concentrated winding, pole-pair number *p*=6 and rotor radius *rra*=80mm) and DWq2-p6rra80 (distributed winding with *q*=2, pole-pair number *p*=6 and rotor radius *rra*=80mm).

As the end winding is smaller than that of the DW geometries, the CW geometries provide a higher torque and power density (larger active length) at lower Ohmic losses, which are independent of speed but only depend on the torque, which is proportional to the current.

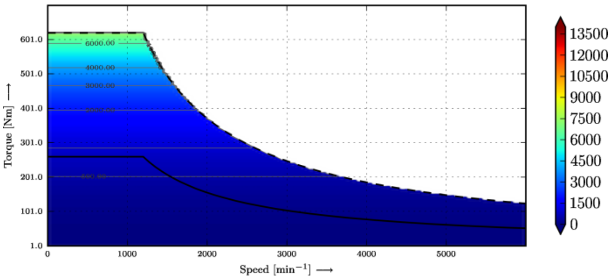

(a) CW- *p6rra80*

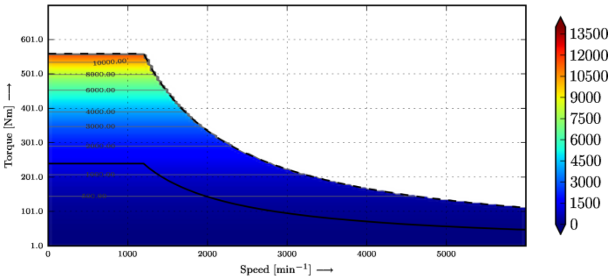

(b) DW*q2-p6rra80*

Fig. 12. Ohmic losses (W).

b) Iron losses

The iron-loss maps for the geometries CW-p4rra75 and CW-p8rra85 are depicted in Fig.13. The rated torque and the overload torque increase with the pole-pair number as could also be seen in the previous section. Iron losses increase with the pole-pair number, since the frequency of the alternating magnetic field increases. The iron losses of the concentrated-winding geometry hardly differ from the iron losses of the

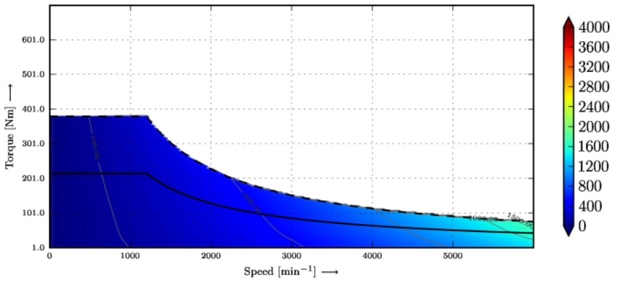

(a) CW-*p4rra75*

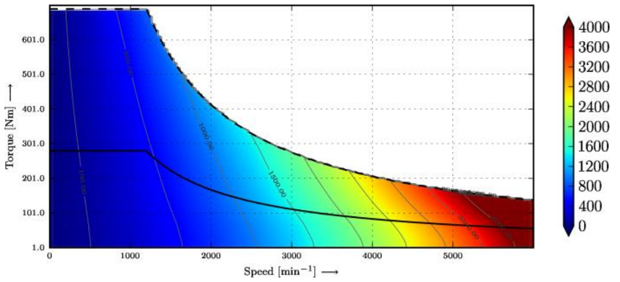

(b) CW-*p8rra85*

Fig. 13. Iron losses (W).

distributed-winding geometry, because the iron's volume remains approximately constant.

c) Magnet eddy-current losses

The eddy-current losses in the permanent magnets are, in a first step, calculated with an axial segmentation of the magnets. Since the skin depth of the magnet's eddy currents is in the range of the magnet's dimensions, the eddy-current losses decrease (similar to the core lamination) as the number of axial magnet division increases, see Fig.14,*a*. As the relative loss difference between two segmentation numbers remains constant against all operation points (end effects are neglected, FE-model without end windings), the calculations are performed with a segmentation number of 12 to keep the computational efforts and the 3D-FE model within reasonable limits. Due to feasibility reasons of later mass production, the axial magnet segmentation of the machine is limited to 4 divisions for prototyping. In Fig.14,*b* and Fig.14,*c* the maps of the eddy-current losses, occurring in the permanent magnets, are depicted for CW-p8rra85 and DWq2-p8rra90.

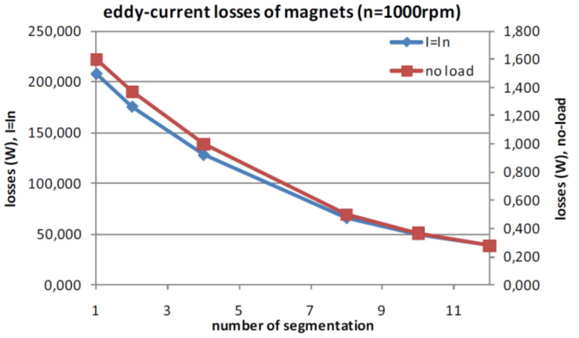

(a) depending on axial segmentation

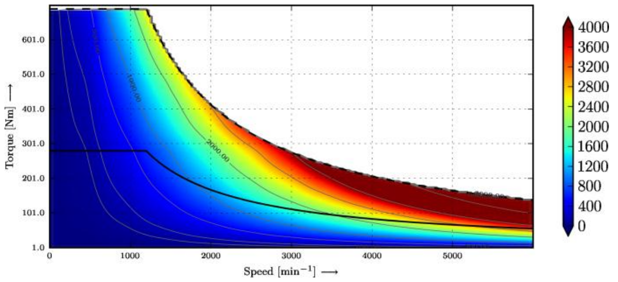

(b) CW-*p8rra85*

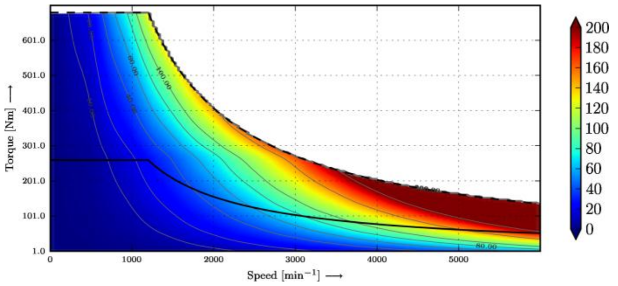

(c) DW-*p8rra90*

Fig. 14. Magnet's eddy-current losses (W).

Eddy-current losses depend on speed ($\sim f^2 \sim (n\,p)^2$) and torque (current), but hardly depend on the pole-pair number, although the frequency increases by raising the pole number. However, by increasing the pole number the magnet's width is decreased ($w_{PM} \sim 1/p$), this damps the eddy currents in the same way as the axial segmentation and the shortening of the magnet's axial length. This damping of the eddy currents compensates a possible increase of the losses caused by the frequency rise, i.e. the eddy-current losses remain constant and are independent of the pole number.

A great difference, however, can be recognized comparing the two stator types. The magnet losses occurring in the distributed-winding geometry are about 20-times smaller when compared to those of the concentrated winding.

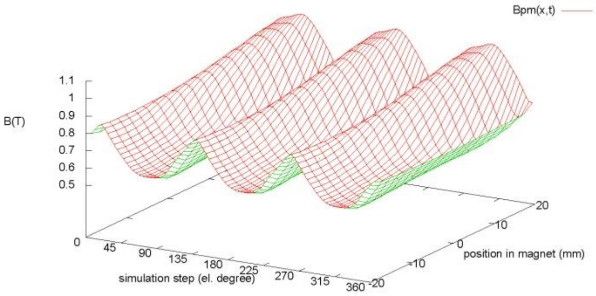

(a) CWp4, nominal load

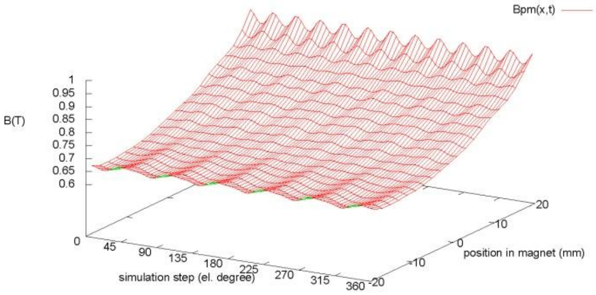

(b) DWp4, nominal load

Fig. 15. The magnetic flux density in the magnets depending on position and time step.

The reason for this becomes evident if the periodic change of the magnetic flux density inside the magnets, which actually causes the

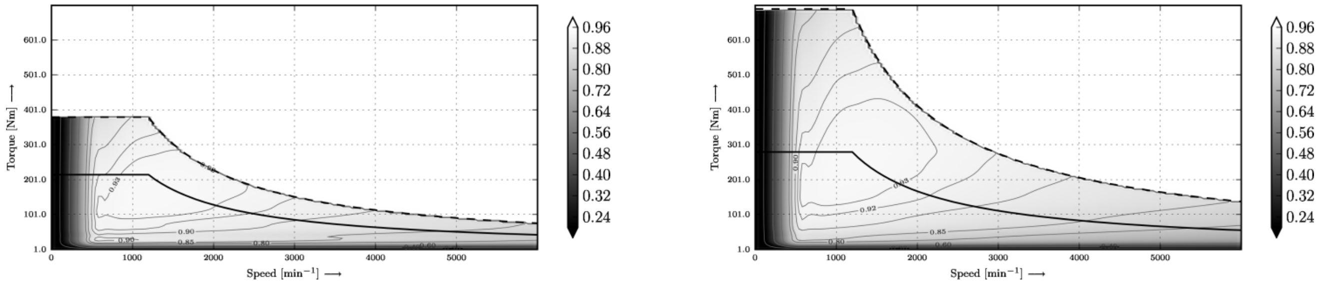

(a) CW*p4rra75** **(b)** CW*p8rra85*

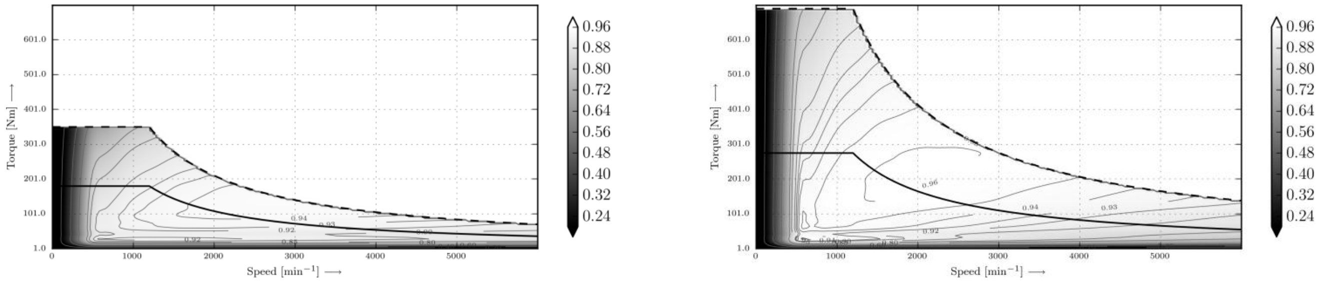

(c) DW*q1p4rra75* **(d)** DW*q1p8rra90*

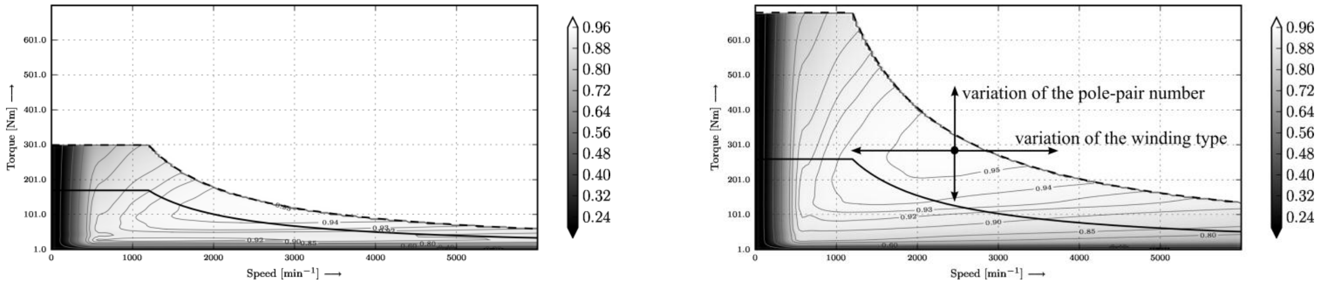

(e) DW*p4rra75* **(f)** DW*p8rra90*

Fig. 16. Efficiency maps.

eddy currents, is regarded. The magnetic flux density depending on position (over magnet width) and simulation step (over an electric period) is depicted in Fig.15 for the no load operation and nominal operation.

d) Efficiency maps

In Fig.16, the efficiency maps are depicted for all stator types and p=4 and p=8.

The efficiency contribution of concentrated-winding geometries has its maximum at lower speeds, whereas the distributed-winding geometries have their maximum efficiency at higher speeds.

As described in preceding sections the application of the concentrated winding decreases the Ohmic losses and increases the eddy-current losses of the machine. Since the Ohmic losses, which remain constant with speed, are the main losses at lower speeds and the eddy-current losses, which increase with f^{2}, are the main losses at higher speeds, the application of the concentrated winding shifts the range of best efficiency to lower speeds.

The application of the distributed winding shifts the range of best efficiency to higher speeds, because it increases the Ohmic losses and decreases the eddy-current losses of the machine.

e) Overall efficiency

The choice of winding type, pole-pair number and thus rotor radius should depend on the vehicle and its intended purpose. Therefore, the overall efficiency depending on named vehicle concepts and driving cycles is determined for each geometry, see Table 1. The best efficiencies for each vehicle concept and driving cycle is emphasized.

Table 1. The overall efficiency depending on vehicle concepts and driving cycle.

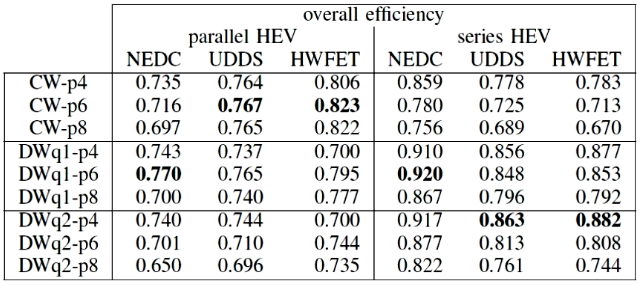

	overall efficiency					
	parallel HEV			series HEV		
	NEDC	UDDS	HWFET	NEDC	UDDS	HWFET
CW-p4	0.735	0.764	0.806	0.859	0.778	0.783
CW-p6	0.716	**0.767**	**0.823**	0.780	0.725	0.713
CW-p8	0.697	0.765	0.822	0.756	0.689	0.670
DWq1-p4	0.743	0.737	0.700	0.910	0.856	0.877
DWq1-p6	**0.770**	0.765	0.795	**0.920**	0.848	0.853
DWq1-p8	0.700	0.740	0.777	0.867	0.796	0.792
DWq2-p4	0.740	0.744	0.700	0.917	**0.863**	**0.882**
DWq2-p6	0.701	0.710	0.744	0.877	0.813	0.808
DWq2-p8	0.650	0.696	0.735	0.822	0.761	0.744

f) Final choice

As one can see, the overall efficiency resulting from the frequency distribution of the machine's operation points and the efficiency map depend on the geometry of the machine, i.e. in this case the winding type and the pole-pair number.

Would the vehicle concept result in a frequency distribution which is limited to a range of lower speeds and higher torques, a concentrated-winding geometry should be preferred, even though the overall efficiency is only little better. This would be the case if applying the parallel HEV of this work, in which the control of automated transmission limits the torque and speed to such a range.

Would the vehicle concept result in a frequency distribution of a wider speed range, the distributed-winding geometry should be preferred. This geometry offers a good efficiency especially at higher speeds due to significant lower eddy-current losses in the permanent magnets.

If the limited space, and therefore the power density, is the main problem the concentrated-winding geometry has to be preferred in any case. Due to its small end winding and increased active length it offers a higher torque and output power (Table 2). In addition, the output power can be raised by increasing the pole-pair number of each machine type, stretching the complete map towards higher speeds. However, since the efficiency at lower torques is decreased by this means, the increase of the pole number just makes sense if the machine would not be oversized.

6. Conclusions

This paper presents a methodology to design an electrical machine and optimize the operational efficiency of PMSM drives under the constraint of limited installation space. Starting with exemplary vehicle simulations, this study demonstrates an approach to determine the optimum rotor radius, the optimum pole pair number and the appropriate winding type of the machine, regarding the machine's rated power, overload capacity and average efficiency, which depends on above-named vehicle simulations.

It is shown that, in order to improve the energy balance and reduce the vehicle's fuel consumption, it is not the maximum efficiency

Table 2. The overall efficiency depending on vehicle concepts and driving cycle.

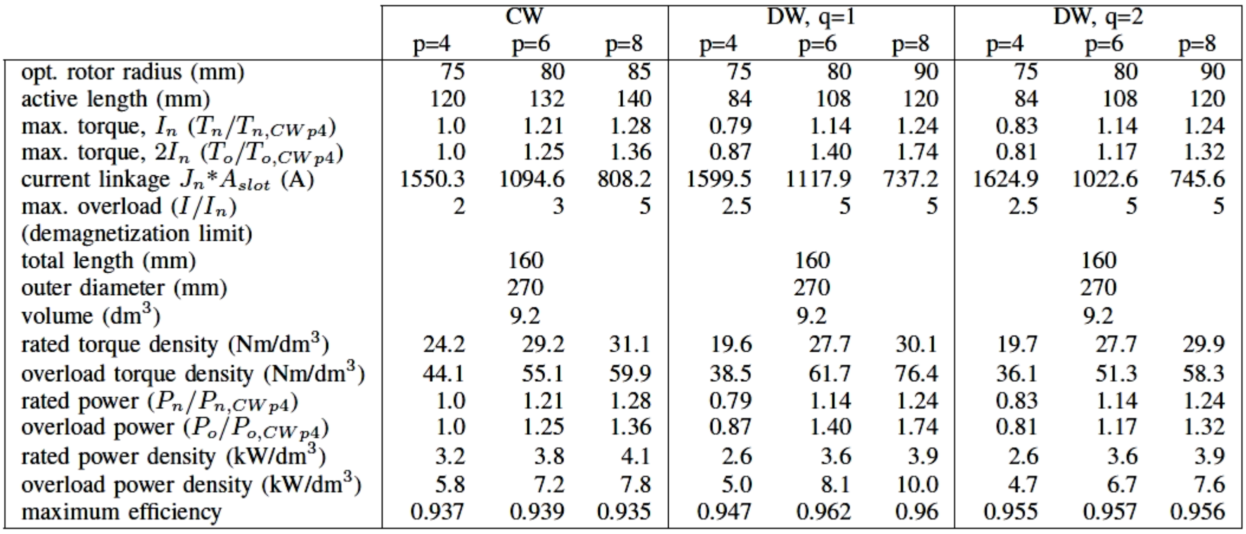

	CW			DW, q=1			DW, q=2		
	p=4	p=6	p=8	p=4	p=6	p=8	p=4	p=6	p=8
opt. rotor radius (mm)	75	80	85	75	80	90	75	80	90
active length (mm)	120	132	140	84	108	120	84	108	120
max. torque, I_n ($T_n/T_{n,CW\,p4}$)	1.0	1.21	1.28	0.79	1.14	1.24	0.83	1.14	1.24
max. torque, $2I_n$ ($T_o/T_{o,CW\,p4}$)	1.0	1.25	1.36	0.87	1.40	1.74	0.81	1.17	1.32
current linkage $J_n{*}A_{slot}$ (A)	1550.3	1094.6	808.2	1599.5	1117.9	737.2	1624.9	1022.6	745.6
max. overload (I/I_n) (demagnetization limit)	2	3	5	2.5	5	5	2.5	5	5
total length (mm)		160			160			160	
outer diameter (mm)		270			270			270	
volume (dm^3)		9.2			9.2			9.2	
rated torque density (Nm/dm^3)	24.2	29.2	31.1	19.6	27.7	30.1	19.7	27.7	29.9
overload torque density (Nm/dm^3)	44.1	55.1	59.9	38.5	61.7	76.4	36.1	51.3	58.3
rated power ($P_n/P_{n,CW\,p4}$)	1.0	1.21	1.28	0.79	1.14	1.24	0.83	1.14	1.24
overload power ($P_o/P_{o,CW\,p4}$)	1.0	1.25	1.36	0.87	1.40	1.74	0.81	1.17	1.32
rated power density (kW/dm^3)	3.2	3.8	4.1	2.6	3.6	3.9	2.6	3.6	3.9
overload power density (kW/dm^3)	5.8	7.2	7.8	5.0	8.1	10.0	4.7	6.7	7.6
maximum efficiency	0.937	0.939	0.935	0.947	0.962	0.96	0.955	0.957	0.956

that decides whether or not a machine design is chosen for application, but the overall efficiency depending on the actual operation.

References

1. M. Zeraoulia, M.E.H. Benbouzid, D. Diallo. “Electric Motor Drive Selection Issues for HEV Propulsion Systems: A Comparative Study”, *IEEE Trans. on Vehicular Technology*, Vol.55, No.6, November 2006.
2. L. Chang. “Comparison of AC Drives for Electric Vehicles - A Report on Experts’ Opinion Survey”, *IEEE AES Systems Magazine*, August 1994.
3. M. Yabumoto, C. Kaido, T. Wakisaka, T. Kubota, N. Suzuki. “Electrical Steel Sheet for Traction Motors of Hybrid/Electrical Vehicles”, *Nippon Steel Technical Report*, No.87, July 2003.
4. J.G.W. West. “Propulsion systems for hybrid electric vehicles”, *Electrical Machine Design for Electric and Hybrid-Electric Vehicles, IEE Colloquium on*, pp. 1/1 - 1/9, October 1999.
5. C.C. Chan. “An overview of electric vehicle technology”, *Proc. of the IEEE*, Volume 81, Issue 9, Page(s):1202 - 1213, September 1993.
6. T. Finken, M. Felden, K. Hameyer. “Comparison and design of different electrical machine types regarding their applicability in hybrid electrical vehicles”, *Proc. of the ICEM*, September 2008.
7. Institute of Electrical Machines, RWTH Aachen University. ”In-house FE package iMOOSE.” Internet: http://www.iem.rwth-aachen.de/index.pl/simulatio design, 2009 [Jan. 28, 2010].
8. G. Bertotti, “General properties of power losses in soft ferromagnetic materials.”, *IEEE Transactions on Magnetics*, Vol. 24, No. 1 p. 621-630, January 1988.
9. G. Bertotti *et al.*, “An improved estimation of iron losses in rotating electrical machines.”, *IEEE Transactions on Magnetics*, Vol. 27, No. 6, p. 5007-5009, November 1991.
10. M. Herranz Gracia, E. Lange, K. Hameyer, “Numerical Calculation of Iron Losses in Electrical Machines with a modified Post-Processing Formula.”, *Proc. of 16th COMPUMAG*, Aachen, 2007.
11. C. Kaehler, G. Henneberger, “An eddy-current computation in the claws of synchronous a claw-pole alternator in generator mode.”, *IEEE Transactions on Magnetics*, Vol. 38, No. 2, p. 1201-1204, March 2002.
12. C. Kaehler, G. Henneberger, “Eddy-current computation on a one pole-pitch model of a synchronous claw-pole alternator.”, *COMPEL - The International Journal for Computation and Mathematics in Electrical and Electronic Engineering*, v 22, n 4, p 834-846, 2003.
13. J.F. Gieras, M. Wing, *Permanent-Magnet Motor Technology*. CRC, 2002.
14. D.C. Hanselman. *Brushless Permanent-Magnet Motor Design*. The Writers’ Collective, 2003.
15. J. Cros, P. Viarouge, “Synthesis of high performance PM motors with concentrated windings.”, *IEEE Transaction on Energy Conversion*, Vol. 17, Issue 2, p. 248-253, June 2002.
16. B. Stumberger *et al.*, “Permanent-magnet synchronous motor with exterior-rotor: distributed or concentrated windings - motor performance comparison.”, *COMPEL - The International Journal for Computation and Mathematics in Electrical and Electronic Engineering*, Vol. 25, Issue 3, p. 721 - 726, 2006.
17. K. Yamazaki, Y. Fukushima, M. Sato, “Loss Analysis of Permanent-Magnet Motors With Concentrated Windings - Variation of Magnet Eddy-Current Loss Due to Stator and Rotor Shapes.”, *IEEE Transactions on Industry Applications*, Vol. 45, Issue 4, p. 1334-1342, July 2009.

Received May 31, 2010

Eng. Thomas Finken
Eng. Martin Hafner
Eng. Matthias Felden
Prof. Kay Hameyer

Institute of Electrical Machines
RWTH Aachen University
Schinkelstr., 4
D – 52056 Aachen, Germany